Y(III) sorption at the orthoclase (001) surface measured by X-ray reflectivity

Neumann, J.; Lessing, J.; Lee, S. S.; Stubbs, J. E.; Eng, P. J.; Demnitz, M.; Fenter, P.; Schmidt, M.;

Originally published:

December 2022

Environmental Science & Technology 57(2022)1, 266-276

DOI: https://doi.org/10.1021/acs.est.2c06703

Y(III) sorption at the orthoclase (001) surface measured by X-ray reflectivity

Julia Neumann[a,b*], Jessica Lessing[a], Sang Soo Lee[b], Joanne E. Stubbs[c], Peter J. Eng[c,d], Maximilian Demnitz[a,±], Paul Fenter[b], Moritz Schmidt[a,*]

[a] *Helmholtz-Zentrum Dresden-Rossendorf, Bautzner Landstraße 400, 01328 Dresden, Germany*

[b] *Argonne National Laboratory, 9700 South Cass Avenue, Lemont, IL 60439, USA*

[c] *Center for Advanced Radiation Sources, The University of Chicago, 929 E 57th Street, Chicago, IL 60637, USA*

[d] *James Franck Institute, The University of Chicago, 929 E 57th Street, Chicago, IL 60637, USA*

[±] *Current address: Eindhoven University of Technology, Het Kranenveld 14, 5612 AZ Eindhoven, Netherlands*

* *Corresponding Authors, E-Mail addresses: jneumann@anl.gov, moritz.schmidt@hzdr.de*

Julia Neumann: jneumann@anl.gov, ORCID: 0000-0002-3650-3967

Jessica Lessing: j.lessing@hzdr.de, ORCID: 0000-0002-6485-4035

Sang Soo Lee: sslee@anl.gov, ORCID: 0000-0001-8585-474X

Joanne E. Stubbs: stubbs@cars.uchicago.edu, ORCID: 0000-0002-8509-2009

Peter J. Eng: eng@cars.uchicago.edu, ORCID 0000-0002-8072-3203

Maximilian Demnitz: m.demnitz@tue.nl, ORCID: 0000-0002-4137-1057

Paul Fenter: fenter@anl.gov, ORCID: 0000-0002-6672-9748

Moritz Schmidt: moritz.schmidt@hzdr.de, ORCID: 0000-0002-8419-0811

ABSTRACT

Interactions of heavy metals with charged mineral surfaces control their mobility in the environment. Here, we investigate the adsorption of Y(III) onto the orthoclase (001) basal plane, the former as a representative of rare earth elements and an analogue of trivalent actinides and the latter as a representative of naturally abundant K-feldspar minerals. We apply *in-situ* high-resolution X-ray reflectivity to determine the sorption capacity and molecular distribution of adsorbed Y species as a function of Y^{3+} concentration, $[Y^{3+}]$, at pH 7 and 5. With $[Y^{3+}] \geq 1$ mM at pH 7, we observe an inner-sphere (IS) sorption complex at a distance of ~1.5 Å from the surface and an outer-sphere (OS) complex at 3–4 Å. Based on the adsorption height of the IS complex a bidentate, binuclear binding mode, in which Y^{3+} binds to two terminal oxygens is proposed. In contrast, mostly OS sorption is observed at pH 5. The observed maximum Y coverage is max. ~1.3 Y^{3+}/A_{UC} (A_{UC}: area of the unit cell = 111.4 $Å^2$) for all investigated pH values and Y concentrations, which is in the expected range based on the estimated surface charge of orthoclase (001).

KEYWORDS: solid liquid interface, rare earth elements, sorption, crystal truncation rod, resonant anomalous X-ray reflectivity, feldspars

Synopsis statement: (approximately 20 words)

The study provides a molecular-scale insight into the facet-specific sorption of Y(III) on orthoclase (001).

TOC:

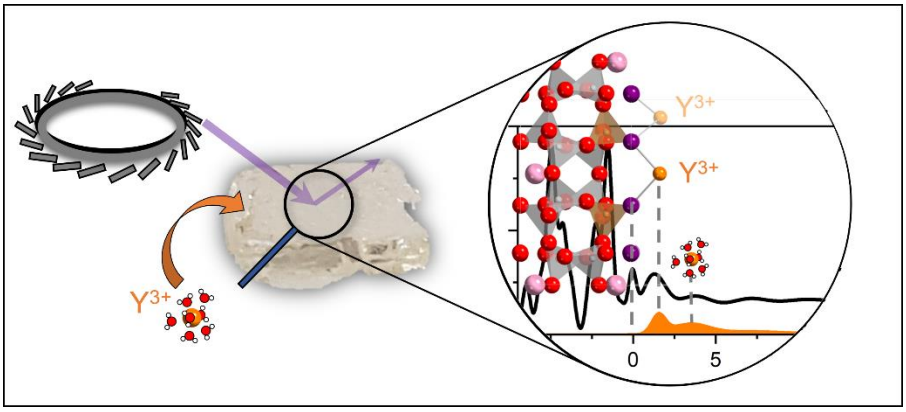

1 Introduction

Heavy metal contaminants are of concern due to their high risks to ecological systems and human health. One group of heavy metals that has been of special interest in the last few decades are rare earth elements (REE), which are essential for modern electronic devices, especially those developed for green technologies.[1,2] Increased demand and use of REEs has led to significant increases in the environmental pollution caused by REE mining, recycling, and electronic waste disposal[3–8], resulting in negative health effects such as oxidative stress in living organisms.[9–11] Especially acid mine drainage leads to high REE concentrations in the environment, with total REE concentrations as high as 17 mg/L at a wide range of pH values from 2 to 7.5.[8,12–15]

The mobility of REEs in the environment is largely controlled by their interactions with mineral surfaces.[16,17] Many studies have been carried out to assess the retention potential of major rock-forming minerals, such as quartz[18–20] and micas[21–26] for trivalent heavy metals M(III), including REEs and trivalent actinides. The impact of pH, metal concentration, and ligands on the adsorption was investigated and models have been developed to predict the fate of REEs.[23,27,28] Mechanistically, studies of ion adsorption on muscovite mica showed that multivalent ions tend to adsorb farther from the mineral surface,[29–31] which is related to multivalent ions' ability to retain water molecules. Some ions, for example Al(III)[32] and some actinides like Pu(III/IV)[33] and Th(IV)[26], polymerize at the interface to form secondary-phase thin films or nanoparticles.

Another naturally abundant group of minerals are feldspars,[34] which are composed of a negatively charged 3D framework of oxygen-bridged aluminosilicate tetrahedra, usually compensated by K^+, Na^+, or Ca^{2+}. Some studies are available on the sorption of trivalent heavy metals on feldspars,[35–38] most of which use mineral powder samples. For example, our group has recently studied the sorption of REEs (Eu, La, Lu, Nd, Y) as well as Am(III) and Cm(III) on K-feldspar powders. By combining batch sorption experiments and time-resolved laser-fluorescence spectroscopy (TRLFS), a generic surface complexation model was developed to

predict the retention of REEs and trivalent actinides.[36] A bidentate coordination for the sorption complex was assumed for this model but could not be verified by the available experimental data.

While studies using mineral powder samples give a solid basis for determination of thermodynamic parameters for surface complexation reactions,[39–41] the development of realistic reactive transport models requires an understanding of facet-specific reactivity,[42] the influence of surface roughness,[38,43,44] and solid-liquid ratios more similar to those in natural systems. Orthoclase ($KAlSi_3O_8$), a common polymorph of K-feldspar, has a monoclinic crystal structure ($a = 8.56$ Å, $b = 12.99$ Å, $c = 7.19$ Å, $\alpha = \gamma = 90°$, $\beta = 116°$)[45] with perfect cleavage planes along the (001) and (010) orientations, which are commonly exposed in natural systems.[46] An illustration of the (001) surface is given in the Supporting Information (Figure S1 in SI). Each unit cell of the (001) surface is terminated by a layer of four aluminosilicate tetrahedra pointing out of the surface plane and exposing terminal oxygens (TOs). There are two symmetry-distinct sites of TOs in the orthoclase (001) unit cell, referred to as TO1 and TO2. Two symmetry-equivalent TO1s and two TO2s are located in the middle and the border of the unit cell, respectively (Figure S1). The TOs are typically hydrolyzed in aqueous solution and are (de)protonated depending on the conditions in the aqueous solution, e.g. pH and ionic strength, causing a pH-dependent surface charge of orthoclase. Furthermore, the orthoclase (001) surface has two cavities that are occupied by K^+, which can be released in contact with water,[47,48] leading to an additional contribution of 2 e^-/A_{UC} (A_{UC}: area of the unit cell, $A_{UC}(001) = 111.4$ $Å^2$) to the maximum surface charge.

Due to its perfect cleavage plane, the orthoclase (001) surface is well suited for investigations of molecular-scale processes, including mineral dissolution[47–50] and ion sorption.[38,51] For the latter, spectroscopy and X-ray scattering techniques allow the discrimination of different sorption modes, which are usually divided based on differences in the degree of adsorbate hydration. Inner-sphere (IS) complexes show a partially removed hydration shell, while for

outer-sphere (OS) and extended outer-sphere sorption complexes the first or multiple intervening hydration layers are preserved.[52]

Studies of ion adsorption on the orthoclase (001) surface report that alkali ions (e.g., Rb^+, Cs^+) undergo a cation exchange with K^+ from the top layer of the mineral surface and adsorb as an IS complex in the K^+ cavities.[51,53] In contrast, experimental and theoretical studies show that alkaline earth ions (Sr^{2+}, Ca^{2+}, Mg^{2+}) form mainly OS complexes due to their relatively stronger hydration.[51,54] Molecular dynamic simulations investigated the hydration structure of the orthoclase (001) and (010) surfaces[55] and sorption of $U(VI)O_2^{2+}$ thereon,[56] and report a transition from an OS to a monodentate IS complex, and eventually to a bidentate, mononuclear IS coordination.

Additionally, we recently investigated the impact of nanoscale surface roughness on the sorption of Cm(III) on an individual K-feldspar crystal of the (001) orientation using spatially resolved luminescence spectroscopy.[38] We find that the surface reactivity depends upon the topographic variation of the K-feldspar surface. Therefore, models describing reactivity based only on sorption studies using mineral powders with uncontrolled defect densities are insufficient for robust environmental transport predictions. While the previously applied spectroscopy is sensitive to changes in the hydration and gives spatially resolved information about the interfacial speciation, it cannot give insight in the molecular scale interfacial structure, e.g., different binding modes of adsorbed species. The structure and binding mode of a complex will, however, directly affect how strongly the adsorbed ion is retained by the interface and is required to establish thermodynamic models of the sorption process. Consequently, we aim to directly determine such interfacial structures by investigating the truly intrinsic reactivity of an ideal defect-free surface by applying surface-sensitive and element-specific high-resolution X-ray reflectivity to get a deeper insight in the sorption structure.

2 Materials and Methods

2.1 Mineral Substrate and Sample Preparation

Gem-quality orthoclase single crystals (transparent with slightly yellow discoloration) were purchased from The Arkenstone Company (mined in Itrongay, Madagascar). The crystals were cleaved, rinsed with deionized water (DIW), and stored in a solution of 0.1 M NaCl at pH 7 to prevent contamination or dissolution.[57] Solutions containing 0.1–10 mM YCl_3 were prepared by dissolving the salt in DIW under atmospheric conditions. The pH value was adjusted by addition of small amounts of 0.01 and 0.1 M HCl or NaOH.

Two different orthoclase (001) crystals (cleaved from the same specimen) were used for the sorption experiments. One crystal was used to explore the impact of dissolved Y^{3+} ion concentration, [Y^{3+}]. The chosen concentration are in the range of, but not limited to the values found in water samples at REE mining sites (< 17 mg/L).[8,12–15] The first crystal was reacted in a solution of 0.1 mM YCl_3 (= 8.9 mg/L) at pH 7 for 18 h of equilibration, after which X-ray reflectivity (XR) was measured. Due to a relatively low surface coverage, two samples at higher Y concentrations were measured. The same crystal used for the experiments at 0.1 mM Y^{3+} was transferred into a solution at a higher [Y^{3+}] = 1 mM at the same pH, reacted for additional 18 h, and XR was measured again. While the Y concentrations are relatively high our previous work on the adsorption of REEs and trivalent actinides on K-feldspar powder showed that a change of metal concentration (in the investigated range of nM–mM) leads only to a shift in the adsorption edge, but not to a change in the molecular adsorption structure.[36] Therefore, insights obtained at higher Y concentrations are still transferable to REE concentrations related to heavy metal contaminated sites (up to 17 mg/L[13]).

A similar experimental approach was chosen for the second crystal, where the impact of pH was investigated at a fixed [Y^{3+}] = 10 mM. After initial reaction at pH 5, XR was measured, and the crystal was then transferred to a 10 mM YCl_3 solution at pH 6.9 (for simplicity referred

to as pH 7) and remeasured. These two chosen pH values are based on the beginning of the sorption edge on K-feldspar powders obtained in the previous study and overlap environmentally relevant pH values in stream waters in tailing of REE mines (4.5–7.5).[8,12,13] Speciation calculations (Visual Minteq, Database NIST46, Critically Selected Stability Constants of Metal Complexes: Version 8.0) for the experimental conditions (10 mM YCl_3 at pH 6.9) show a saturation index of +0.361, suggesting a slight oversaturation of $Y(OH)_3$. However, precipitation of Y-containing solid phases was not observed visually during the preparation of the solutions. In addition, no evidence for crystalline precipitates was observed (either as oriented precipitates that would lead to Bragg peaks that are superimposed on the specular rod, or as randomly oriented precipitates that would appear as "powder rings" that would appear in the background signals) during X-ray measurements.

2.2 X-ray Reflectivity Experiments

We used two variations of high-resolution X-ray reflectivity. The first one is specular crystal truncation rod (CTR) diffraction, a type of surface X-ray diffraction.[58] CTRs are continuous lines of scattering intensity perpendicular to surfaces and are several orders of magnitude weaker than Bragg peaks. Specular CTR analysis enables the determination of the total electron-density profile of the mineral/water interface. The second method is resonant anomalous X-ray reflectivity (RAXR),[59] which is element-specific and probes the interfacial distribution of a specific element.

CTR and RAXR experiments. X-ray data were measured at beamline 13-ID-C (GeoSoilEnviroCARS) at the Advanced Photon Source (APS) at Argonne National Laboratory.[60] A thin-film cell[61], containing a reacted orthoclase crystal (see above) with its cleaved (001) surface exposed, was filled with ~50 µL of sample solution and closed with a 7.5 µm Kapton film, holding the crystal in place while maintaining a thin layer (several µm) of

the solution on the crystal surface. To minimize any solution evaporation through the Kapton window, and therefore changes in [Y^{3+}] during the measurement, an additional Mylar dome filled with water-saturated He was placed on the sample cell. Potential beam-induced alteration of the mineral surface was monitored by repeatedly measuring smaller parts of the CTR and RAXR data throughout the entire measurement. No significant changes were observed.

The incident X-ray beam was collimated using a pair of 1-meter-long Si mirrors in Kirkpatrick-Baez geometry, and the final size was adjusted by slits to a size of 0.05–0.25 x 0.5–1.0 mm^2 with an average flux of ~10^{12} photons per second at the sample position. The scattering data was measured in the horizontal plane using a Newport six-circle diffractometer and a Dectris PILATUS 100K 2D pixel array detector.[62]

Specular CTR data were measured with an X-ray energy of 14.0 keV that is far from the Y K-edge (17.038 keV, determined by X-ray absorption spectroscopy of a sample in fluorescence mode). CTR measures the X-ray reflectivity signal, R(q), as a function of momentum transfer magnitude, q (0.3–6.0 $Å^{-1}$), which is related to the scattering angle 2θ through the relation:

$$q = 2\cdot|\vec{k}|\cdot\sin\left(\frac{2\theta}{2}\right) = \frac{4\pi}{\lambda}\cdot\sin\left(\frac{2\theta}{2}\right) \quad \text{(Eq. 1)}$$

Here, $\vec{k}$ is the wave vector with $|\vec{k}| = 2\pi/\lambda$ and λ (= 0.886 Å) is the X-ray wavelength.

Element-specific structural information is obtained from RAXR spectra that probe X-ray reflectivity signal (at 10–11 different fixed values of momentum transfer) as a function of X-ray energy through the X-ray absorption edge of the resonant element. Here the Y(III) K absorption edge is at 17.038 keV. Data analysis requires the determination of resonant anomalous dispersion terms $f'(E) + if''(E)$, which were obtained by the measurement of X-ray absorption spectroscopy (XAS) from one of the samples using a SII Vortex ME4

fluorescence detector, followed by a Kramers-Kronig transformation. More details are provided in the literature.[22,63]

XR Data Analysis. Here, only a brief description of XR data analysis is given, and more details can be found in Section 2 of the SI and in the literature.[58,64,65] The reflectivity *R* of a given interfacial structure is proportional to the squared value of the structure factor modulus *F* and can be calculated from the atomic scattering factors $f_j(q)$:

$$R(q) \sim |F(q)|^2 = \left| \Sigma_j c_j f_j(q) \cdot \exp(iqz_j) \cdot \exp\left(-\frac{(qu_j)^2}{2}\right) \right|^2 \quad \text{(Eq. 2)}$$

Individual atomic layers in Eq. 2 are expressed as *j* Gaussian peaks with an occupancy c_j, distance from the surface z_j, and a root-mean-square (rms) width u_j. The model structure consists of the orthoclase bulk structure, an interfacial layer (d_{001} = 6.484 Å)[45], and several layers of adsorbed species including water molecules. Each data set is analyzed by simulating the reflectivity for a given structural model and optimizing the model parameters using a least-squares fitting routine based on the scaled χ^2 and R-factor (see Section 2 in SI). The CTR data then reveal a total electron density profile in the direction normal to the orthoclase (001) surface.

The analysis of the resonant data followed a similar approach. Each RAXR spectrum, *R(q,E)* at a fixed *q*, is calculated from the total structure factor *F* that is the sum of a non-resonant component (F_{NR}), which is known from the CTR analysis, and a resonant structure factor F_R:

$$R(q,E) = |F(q,E)|^2 = |F_{NR}(q) + F_R(q,E)|^2 \quad \text{(Eq. 3)}$$

$$F_R(q,E) = \left(f'(E) + if''(E)\right) \cdot \Sigma_j c_j \cdot \exp(iqz_j) \cdot \exp\left(-\frac{(qu_j)^2}{2}\right) \quad \text{(Eq. 4)}$$

$$F_R(q,E) = \left(f'(E) + if''(E)\right) \cdot \mathrm{A}(q)\, \exp(\mathrm{i}\Phi(q)) \quad \text{(Eq. 5)}$$

In equation 4 and 5, F_R is defined as the product of $f'(E) + if''(E)$ and the partial resonant structure factor of the resonant atom. Using this expression, the parameters describing the distribution of the resonant species (Y^{3+}) is obtained by least-squares optimization.

3 Results & Discussion

3.1 Reflectivity Data

CTRs. First, the impact of Y^{3+} concentration ([Y^{3+}] = 0.1 – 10 mM) at pH = 7 on the adsorption on orthoclase (001) was investigated by CTR. The measured data are displayed in **Figure 1**. Generally, the non-resonant reflectivity of all samples is very similar to that of the previously published CTR data of the orthoclase (001)–water interface.[66] At $q < 3$ Å^{-1}, the reflectivity for the samples containing Y^{3+} is slightly lower than that for orthoclase in DIW, while the differences for $q = 4$–5 Å^{-1} are mostly within the statistical uncertainty of the datapoints. When comparing the reflectivity between the datasets at 0.1 and 1 mM Y^{3+}, which were measured on the same crystal, the observed changes in the reflectivity signal are most pronounced at the higher [Y^{3+}], which is likely due to an increasing amount of adsorbed Y^{3+} on the surface.

The sorption of Y^{3+} was also investigated at two pH values (5 and 7, **Figure 1**). These pH values were chosen based on our previous powder study, which showed significant changes in sorption quantity and structure within this pH range.[36] The observed trends in the variation of the CTR intensity for the two investigated pH values are similar to those for the aforementioned Y^{3+} concentration series, i.e., decreasing reflectivity for $q < 3$ Å^{-1}.

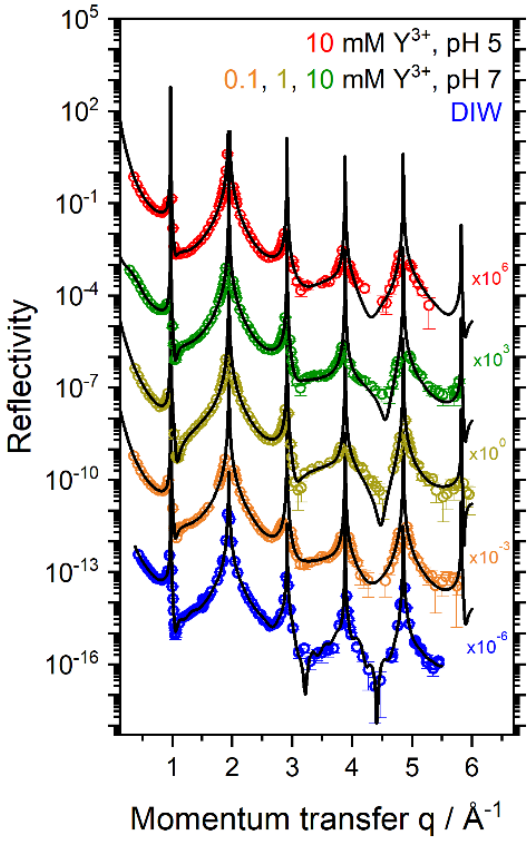

Figure 1. Non-resonant specular X-ray reflectivity of orthoclase (001) surfaces reacted with Y^{3+}-containing solutions at pH 5 and 7 at three different Y^{3+} concentrations (0.1, 1, and 10 mM) displayed using a vertical offset given next to each data set. For comparison the previously reported reflectivity data for the orthoclase (001) surface in DIW is added in blue.[66]

RAXR spectra. RAXR measurements were performed to probe the adsorbed distribution of Y^{3+} at the orthoclase (001) surface. All samples show RAXR modulations at the Y(III) X-ray absorption edge at 17.038 keV (Figures S3 and S4 in SI), showing larger differences between the samples than observed in the CTR data. A model-independent analysis of the RAXR spectra was used to obtain the amplitude A_R and phase Φ_R of the partial resonant structure factor (after Eq. 5, **Figure 2** symbols).[67] Also shown in **Figure 2** is the *q*-dependent variation of A_R and $\Phi_R(q)/q$ (lines) calculated from the best-fit models of the RAXR spectra (model-dependent analysis, cf. **Table 1**).

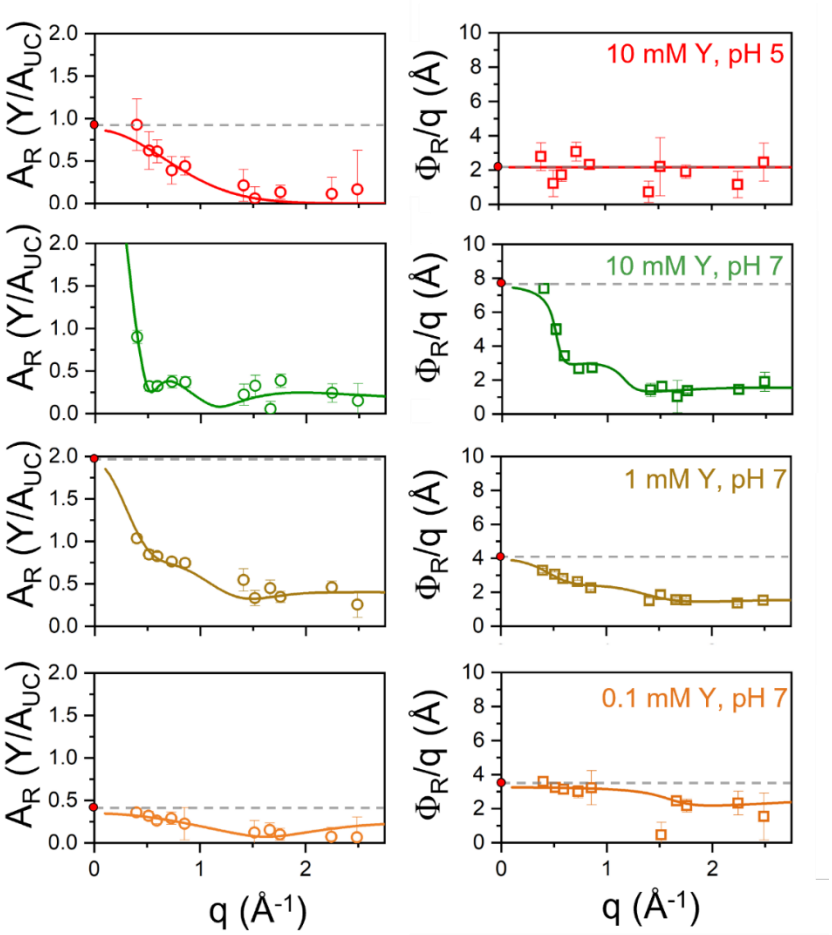

Figure 2. Amplitudes $A_R(q)$ (left) and phase $\Phi_R(q)/q$ (right) of the element-specific partial structure factors F_R as a function of momentum transfer q determined by model-independent (data points) and model-dependent (solid lines, cf. **Table 1**) analyses of RAXR spectra. The average sorption height $\bar{z}$ and total Y coverage θ_{tot} of the adsorbed Y distribution can be estimated from the values of $A_R(q)$ and $\Phi_R(q)/q$ in the limit of $q \rightarrow 0$. The determined values based on best-fit models are indicated by dashed lines and filled, red dots.

Two primary characteristics of the Y-distribution can be inferred directly from the RAXR spectra: the Y-coverage and its average height. The total coverage θ_{tot} can be estimated by the asymptotic value of $A_R(q)$ in the limit of $q \rightarrow 0$.[67] From this we observe that θ_{tot} increases with increasing $[Y^{3+}]$ from ~0.4 to > 1 Y^{3+}/A_{UC} for $[Y^{3+}]$ = 0.1, 1, and 10 mM at pH ~7 (**Figure 2** left panel). The average Y^{3+} sorption height $\bar{z}$ can be estimated by the value of $\Phi_R(q)/q$ in the limit of $q \rightarrow 0$ (i.e., $\bar{z} \approx \frac{\Phi(q)}{q}|_{q\rightarrow 0}$).[67] The data suggest that $\bar{z}$ ~ 3–4 Å at $[Y^{3+}]$ = 0.1 and 1 mM at pH 7 (**Figure 2**, right panel), values that are both small and similar in magnitude, suggesting an adsorption mode close to the surface. This result indicates that the Y^{3+} uptake differs between

the two samples (0.1 to 1 mM Y^{3+}), but no significant modifications in adsorbed ion speciation are observed, supporting the transferability of the observed speciation information to lower metal concentrations.

When [Y^{3+}] is further increased to 10 mM, the adsorbed Y^{3+} is located on average farther from the surface, which can be seen from an increase of $\Phi_R(q)/q$ from ~3–4 Å to ~8 Å. At 10 mM Y^{3+} at pH 5, an intermediate coverage of ~1 Y^{3+}/A_{UC} is observed and $\bar{z}$ is ~2 Å, which indicates that Y^{3+} adsorbs on average closer to the surface at the lower pH. At first glance, this could be interpreted as a larger amount of IS sorption for this condition. However, a detailed analysis of the speciation at pH 7 (described below) indicates the existence of multiple species, and therefore, the conclusion that Y^{3+} adsorbs generally closer to the surface at low pH is misleading.

3.2 Interfacial Structures and Adsorption Speciation of Y

The measured CTR and RAXR data were analyzed to extract the total and Y-specific vertical electron density profiles of the orthoclase (001)–solution interface. The interfacial total electron density profiles of the models that reproduced the CTR data best are displayed in **Figure 3** (lines). Their structural parameters are summarized in Table S1 in the SI. The best-fit models of the orthoclase–water interface all show surface-normal electron density profiles with an ideally terminated surface orthoclase unit cell, the TOs at z ~0 Å, followed by a well-defined peak, which is located for all samples at a distance of 1.3–1.6 Å. This peak, which is similar to the one reported for the orthoclase (001)–water interface by Fenter et al.[66], can be attributed to adsorbed water, which shows oscillatory features at larger distances up to ~7 Å from the orthoclase surface.[68]

An important aspect of the structure for interpretation of the surface charge is the coverage of the outermost K^+-ions. The experimental data could only be fitted satisfactorily when the

occupancy of the top K layer was reduced to a partially occupied layer, which is consistent with exchange of Na^+ against K^+ during storage of the crystals in NaCl and/or the release of Na^+/K^+ from the mineral when the surface becomes hydrated.[66] A more detailed description of the influence of this parameter on the fit is given in Section 5 in the SI. In brief, the best-fit models were obtained for a half occupied top K layer, corresponding to an occupancy of ~1 K_{top}/A_{UC} (see Tables S1 and S4 in SI). However, CTR is not an element-specific technique, and therefore it is not possible to distinguish between Na^+/K^+ and H_3O^+ in the top layers. This leads to the conclusion that the $c(K_{top})$ values given in Tables S1 and S4 are likely overestimated and provide only a lower limit for the K^+ release for an estimation of the surface charge (1–2 e^-/A_{UC}) caused by cation exchange.

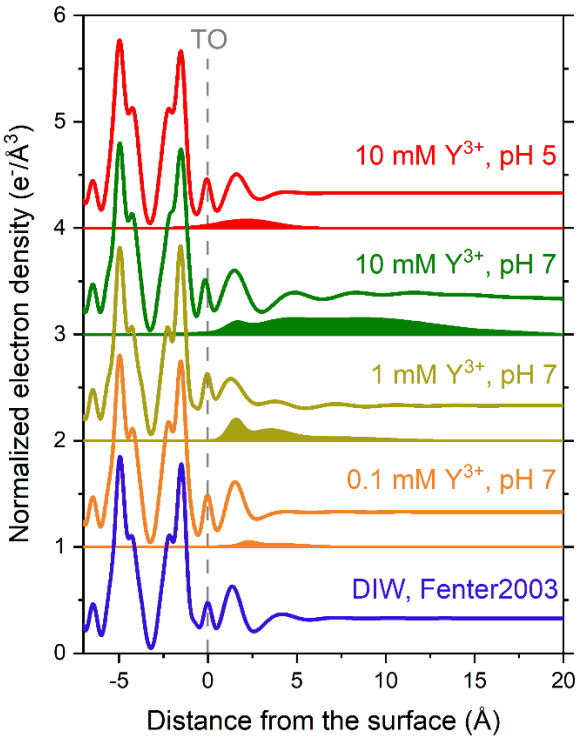

Figure 3. Best fit models of CTR and RAXR data of Y^{3+} adsorbed to orthoclase (001). The total electron density profiles (lines) and Y^{3+} contributions (filled areas) are displayed with a vertical offset of 1 $e^-/Å^3$ for each sample. The interfacial structure of orthoclase (001) in DIW (blue) was adopted from Fenter et al. for comparison.[66] TO marks the terminal oxygen groups, which are defined as crystal surface (z = 0 Å, unrelaxed positions) in our structural model.

Adsorbed Y speciation at pH 5. The electron density profiles of adsorbed Y^{3+} are displayed as filled areas in **Figure 3**. A summary of the parameters of the best-fit models of the RAXR data is provided in **Table 1**. The best fit ($\chi^2 = 0.93$) Y distribution at 10 mM Y^{3+} at pH 5 is described with a single broad peak with an occupancy of 0.86 ± 0.22 Y^{3+}/A_{UC} centered at 2.2 ± 0.2 Å. Other more complex models (e.g., with 2-peak adsorption structures) were explored for but did not yield better fit results (see Section 4.1 in SI). Interestingly, this adsorbed structure is very similar to the findings of a previous study on the adsorption of Sr^{2+} on orthoclase (001), for which an adsorbed amount of 0.74 ± 0.04 Sr^{2+}/A_{UC}, centered at 2.00 ± 0.05 Å under similar experimental conditions (10 mM $SrCl_2$, pH 5.3) was observed (note that for comparison we recalculated the literature coverages because values in the previous study were reported for ½ of the orthoclase unit cell).[51] This species was interpreted to be mainly an OS complex, with a possible small contribution of IS, but the distinction between these scenarios was beyond the experimental resolution of the data. Therefore, at pH 5 the adsorbed Y^{3+} species can be interpreted to be mainly OS, which is consistent with the previous prediction from the surface complexation models for K-feldspar powders.[36] One possible explanation for the poorly defined sorption structure at this pH may be the physical separation of the two K^+ cavities, which are mainly responsible for the surface charge at pH 5. In contrast to IS complexes, OS species are expected to have a higher mobility and therefore less kinetic hindrance for (partial) de/rehydration, allowing less-ordered adsorption in an intermediate position between the two K^+ sites.

Table 1. Measured Y(III) coverages (θ_{tot}) by RAXR, as well as details of the best fit models of RAXR spectra of orthoclase (001) samples reacted in a solution of 0.1–10 mM YCl_3 at pH 5 and 7.

[Y] (mM)	**0.1**	**1**	**10**	**10**
pH	**7**	**7**	**7**	**5**
θ_{tot} (Y/A_{UC})	0.43(15)	1.82(84)	5.3(19)	0.86(22)
IS Species				
z_1 (Å)	-	1.54(6)	1.56(14)	-
c_1 (Y/A_{UC})	-	0.55(8)	0.28(4)	-
u_1 (Å)	-	0.30*	0.30*	-
OS Species				
z_2 (Å)	2.26(26)	-	-	2.17(20)
c_2 (Y/A_{UC})	0.11(3)	-	-	0.86(22)
u_2 (Å)	0.30*	-	-	1.52(33)
z_3 (Å)	3.74(40)	3.43(32)	4.11(18)	-
c_3 (Y/A_{UC})	0.32(12)	0.72(34)	0.60(30)	-
u_3 (Å)	1.66(62)	1.04(33)	1.29(48)	-
Additional Species				
z_4 (Å)	-	7.0(17)	8.67(45)	-
c_4 (Y/A_{UC})	-	0.55(42)	4.4(16)	-
u_4 (Å)	-	2.5(14)	4.09(56)	-
Goodness of Fit				
χ^2	1.06	0.99	1.06	0.93
R-factor (%)	4.4	3.5	1.6	3.0

θ_{tot}: Total coverage (in Y/A_{UC}), z: height (Å) from the orthoclase surface, *c*: occupancy (Y/A_{UC}), and *u*: rms width (Å) of the Gaussian peaks. *fixed value. Errors are reported in brackets.

Adsorbed Y speciation at pH 7. In contrast, the variation of $A_R(q)$ and $\Phi_R(q)/q$ for the samples at near neutral pH clearly indicate the presence of multiple adsorbed Y^{3+} species. The Y electron density at the lowest investigated [Y^{3+}] (0.1 mM, **Figure 3**) is broadly distributed and is described by two peaks, one at 2.3 ± 0.3 Å and the other at 3.7 ± 0.4 Å, with a total Y coverage of 0.43 ± 0.15 Y/A_{UC}. The first peak has a similar distance from the surface as the species described above for pH 5. Therefore, it probably represents here also an OS species with a small contribution of an IS complex, which cannot be distinguished from the OS species at such small amounts.

Higher coverages are obtained at 1 and 10 mM Y^{3+}. The first peak is located at a distance of ~1.55 ± 0.10 Å from the TO planes for both samples. This value indicates that the first hydration shell of the Y^{3+} aquo ion (2.36 Å)[69] was partially removed and therefore this peak represents an IS complex. The rms width of this species was fixed at a small value (0.3 Å) to represent a well-defined adsorption height. The IS complex has a rather small (< 30 % of θ_{tot}) contribution to the overall Y electron density with a coverage of < 0.6 Y^{3+}/A_{UC} (cf. **Table 1**). A second peak is located at larger distances from the orthoclase surface, centered at ~3–4 Å from the TOs. The observed distance is between the radii of the first and second hydration shells (2.36 and 4.40 Å)[69] of the Y^{3+} aquo ion, and would therefore be consistent with an OS sorption complex. This distance is slightly larger than distances of the OS complex found at low pH, but in good agreement with values reported for OS complexes of Y^{3+} on muscovite (4.1–4.3 Å).[70]

The fit quality for the datasets at 1 and 10 mM YCl_3 at pH 7 was improved by including a third species (see Section 4.2 in SI). This additional species is characterized by its large and poorly defined distance from the surface extending up to large distances (10–20 Å) from the surface. While for 1 mM Y^{3+} this species still has a low occupancy (0.55 ± 0.42 Y/A_{UC}), at 10 mM Y^{3+} a large quantity of adsorbed Y of 4.42 ± 1.56 Y/A_{UC} is present in this form. Although only one RAXR spectrum, at lowest measured q = 0.4 $Å^{-1}$, indicates the very high Y coverage of > 1 Y/A_{UC} for the dataset at 10 mM (see **Figure 2**), the very broad distribution of Y electron density is supported by three data points in the phase plot (q < 0.6 $Å^{-1}$), making the fit results reasonably robust.

It should be noted that the experimental conditions for the 1 and 10 mM solutions were close to the solubility limit of $Y(OH)_3$ (see Experimental section for details). The sample surface was mounted on the diffractometer vertically, meaning that precipitates would not deposit onto the crystal surface by sedimentation. However, precursors of the hydroxide phase in the solution could be attracted to the surface, depending on their charge. In addition, it cannot be excluded that locally increased [Y^{3+}] concentrations at the interface induced a heterogeneous formation

of an amorphous $Y(OH)_3$ surface precipitate, causing the large contribution of this species to the Y electron density. However, the CTR data do not show any evidence for any crystalline precipitates on the orthoclase (001) surface.

It should be pointed out here that the estimated $\bar{z}$ in the $\Phi_R(q)/q$ plot (cf. **Figure 2** right) was larger at pH 7 (> 3 Å) than at pH 5 (~2 Å), which could be misinterpreted as adsorption species moving farther away from the mineral surface with increasing pH. However, this is only partially true since $\bar{z}$ represents the average height of adsorbed Y species. While at pH 5, only one OS species is observed and therefore $\bar{z}$ matches z given in **Table 1**, this is not the case for the sample at pH 7, where several species are present. The contribution of additional species far away from the surface at pH 7 leads to the observed $\bar{z}$ of ~8 Å. However, the detailed analysis of the RAXR data shows the presence of a well-defined IS complex (1.55 Å), which is in fact adsorbed closer to the surface than the OS complex (2.17 Å) found at pH 5.

Y coverage. The obtained total and species-specific coverages are summarized in **Table 1**. Overall, Y coverages at pH 7 increase as expected from 0.43 ± 0.15 to 1.82 ± 0.84 and 5.30 ± 1.90 Y^{3+}/A_{UC} with increasing Y^{3+} concentration of 0.1, 1, 10 mM Y^{3+}, respectively. An increase of the pH value also leads to a strong increase of the total Y coverage at 10 mM Y^{3+} from 0.86 ± 0.22 Y^{3+}/A_{UC} at pH 5 to 5.30 ± 1.90 Y^{3+}/A_{UC} at pH 7. The error bars of the coverages are relatively large, especially for samples with high coverages. This is mostly caused by the large uncertainty of the species at large distances from the surface. Therefore, we conservatively estimate the adsorbed Y^{3+} coverage as a range using the sum of the IS and OS coverages, i.e., 0.4 – 1.2 Y/A_{UC}. The additional Y sorbed farther from the surface than the IS and OS complexes may be due to the initial onset of precipitation (cf. additional species in **Table 1**). The trends in Y^{3+} uptake identified for changes in pH and $[Y^{3+}]$ are consistent with the trends described in previous studies on K-feldspar powder, which show increased sorption with increasing metal concentration and pH.[35–37]

3.3. Structure of the Inner-Sphere Sorption Complex

X-ray reflectivity was used to gain insight into the sorption structure of Y(III) on the orthoclase (001) surface. An IS complex at a distance of ~1.5 Å from the TO plane was identified based on the RAXR results. From this observation certain binding geometries of the IS complex can be excluded (see Section 6 in SI for illustrations): (1) No Y electron density was found for $z < 0$, indicating that direct cation exchange at the K^+ site, similar to the previously reported mechanism for Rb^+,[51] is not observed in the case of Y^{3+}. Although the ionic radius of Y^{3+} is smaller (Y^{3+}_{CN9} = 107.5 pm, Rb^+_{CN9} = 163 pm),[71] its large and strongly bound hydration shell presumably makes cation exchange in the K^+ cavity energetically unfavorable. (2) A tridentate or even higher denticity of the sorption complex is unlikely to form on the orthoclase (001) surface. The distances between the TOs are large (5.10 – 8.54 Å, see Figure S1 in SI), which would lead to very long Y-O bond lengths in the sorption complex. (3) A bidentate, mononuclear sorption complex, as observed for UO_2^{2+} experimentally for orthoclase powder[72] and theoretically (MD simulations) also for the (001) surface[56] seems unreasonable, since each aluminosilicate tetrahedron has only one TO on the (001) surface and therefore, the second bond would correspond to a bridging oxygen. Based on the observed average sorption height of ~1.5 Å, a bidentate, mononuclear sorption complex would require a very asymmetric sorption complex with an unrealistically long bond to the bridging oxygen of 3.8 Å (Figure S9 in SI) as compared with the typical Y-O distance of ~2.2–2.5 Å observed in many Y-containing oxides.[73,74] (4) Last, a monodentate, mononuclear sorption complex, in which Y^{3+} forms a chemical bond with one of the TOs, with a relatively short Y-O bond length of ~1.5 Å also seems unlikely (Figure S10 in SI).

The results presented in this study therefore suggest that the Y binding motif is a bidentate, binuclear sorption complex in one of two surface locations: (A) with Y^{3+} located between the two symmetry-equivalent TO1s (Site A, d(TO1–TO1) = 3.72 Å) in the middle of the (001) unit

cell shown in Figure S11, or (B) between TO1 and TO2, with d(TO1–TO2) = 5.10 Å (Site B, Figure S12 in SI). Considering the vertical distance from the TO layer of ~1.5 Å, simple geometric calculations can estimate the Y-O bond length in such a triangular complex, resulting in values of 2.46 Å for Site A and 3.05 Å for Site B. In particular, the value for Site A is in the same range as observed for IS sorption complexes of lanthanides and Am(III) on γ-Al_2O_3 and clay minerals (2.28–2.50 Å)[75], making this binding geometry the most plausible. However, further studies will be needed to support this suggestion with experimental data. This could for example be achieved by the measurement of off-specular X-ray reflectivity data, which could identify laterally ordered structures and therefore, enable the determination of a three-dimensional binding geometry of sorption complexes.[76,77]

3.4. Orthoclase Surface Charge and Compensation by Adsorbed Ions

The results presented in this study enable insights into the orthoclase surface charge, which originates from two different sources: (1) The pH-independent release of K^+ from the surface layer, which was observed to be between ~50–100 % of the 2 K_{top}/A_{UC}. Therefore, the contribution of this source of charge can be estimated to be ~1–2 e^-/A_{UC}, which corresponds to -0.14–0.28 C/m^2. (2) A pH-dependent surface charge of the 4 TOs/A_{UC} that can be deprotonated at high pH, theoretically leading to an additional 4 e^-/A_{UC} if they were to fully deprotonate. Considering these two factors, the charge of orthoclase (001) can theoretically be as high as 6 e^-/A_{UC} or -0.84 C/m^2, which is much higher than reported values for crystallographic planes of other common mineral phases, e.g. -0.02 C/m^2 for calcite (104)[78], -0.11 C/m^2 for quartz (101) at pH 9.8[79] or -0.34 C/m^2 for the muscovite (001) basal plane.[25] While the high surface charge of orthoclase (001) induces a high potential to retain cationic species, the theoretical maximum surface charge is probably not achieved due to electrostatic repulsion between the negative charges.

In more detail, at pH 5 only ~30 % of surface TOs are expected to be deprotonated, indicating that the contribution of pH-dependent surface charge will be small (~1 e^-/A_{UC}, see Section 7 of SI).[36,51] Under these conditions higher quantities of species that keep large parts of their hydration shell, i.e. OS species, are observed. It can therefore be concluded that in the case of orthoclase the negative surface charge is an important driving force to replace water molecules from the coordination sphere and form IS complexes. The coverage at pH 5 is 0.86 Y^{3+}/A_{UC}, which can compensate as much as 2.58 e^-/A_{UC}. At pH 7, ~60 % of the TOs are deprotonated and therefore their contribution to pH-dependent surface charge is more significant (~2.4 e^-/A_{UC}). The estimated total surface charge at pH 7 is ~3.4–4.4 e^-/A_{UC} and the theoretical amount of adsorbed Y^{3+} needed for surface charge compensation is ~1.13–1.47 Y^{3+}/A_{UC}. The RAXR results for the sample at 1 mM Y^{3+} at pH 7 show a total uptake of 1.27 ± 0.42 Y^{3+}/A_{UC} (not considering the contribution of species 3 for the reasons mentioned in Section 3.2), which is in the expected range and indicates full compensation of the estimated surface charge.

It is interesting that a monolayer of the bidentate IS complex with the proposed structure that has two equivalent bidentate sites/A_{UC} would theoretically lead to a maximum IS coverage of 2 Y^{3+}/A_{UC}. However, the RAXR data clearly show that in fact the coverage of the IS complex is relatively low, with values of < 0.6 Y^{3+}/A_{UC}, meaning that only ~ 30 % of available bidentate sites are occupied by IS complexes.

3.5. Current Understanding of Adsorption of Trivalent Heavy Metal Ions on Feldspars

Batch sorption studies. At this point, a comparison to available literature studies provides a comprehensive view on the adsorption of trivalent heavy metal ions on K-feldspar. First, our study was able to shed light on the molecular structure of the formed IS complex. The single type of bidentate IS complex found here is consistent with spectroscopic results reported in our

previous study using K-feldspar powder, in which one type of IS complex and its two hydrolysis forms (which would be indistinguishable for X-ray reflectivity) were identified.[36] Moreover, for surface complexation modeling of the K-feldspar powder, a bidentate coordination of the IS complex was assumed based on the fact that this is often described to be the most common case[80] and yielded reasonable and robust results. Our newest findings on the sorption structure support this assumption and underline the robustness and reliability of the developed surface complexation model, confirming that molecular level studies on single-crystal model systems can be employed to understand powder studies. The major difference is found in the ratio of IS to OS species, which depends strongly on the ratio of available adsorption sites to metal ions in solution. Powder studies usually show higher amounts of IS sorption due to the large excess of surface area of the mineral powder leading to 100 % metal uptake from solution.

Single crystal studies. The results can also be compared to the only study available for sorption of Cm^{3+} on macroscopic K-feldspar crystals,[38] combining autoradiography for quantification of Cm uptake and TRLFS for structural investigations of the sorption complexes. Although the comparability is limited due to differences in metal concentration (1 µM Cm^{3+} vs. 0.1–10 mM Y^{3+}), measurement mode (*ex situ* for TRLFS, where sample preparation partially desorbs OS sorption complexes,[21,81] and *in situ* for (XR), and surface roughness, a few general similarities and differences can be identified: (1) The observed total coverages from both analysis techniques are in the same order of magnitude. TRLFS reported ~0.3 Cm^{3+}/nm^2 at pH 5.5 and ~1.4 Cm^{3+}/nm^2 at pH 7 for areas of 'smooth' surface topography and the adsorbed amount of Y^{3+} found by RAXR is ~0.84 Y^{3+}/nm^2 at pH 5 and ~0.4 – 1.3 Y^{3+}/nm^2 at pH 7 (not considering the species at large distance from the surface), depending on [Y^{3+}]. (2) Regarding the speciation of adsorbed Y^{3+}, Demnitz et al. report a continuous distribution of adsorbed Cm species with 1–9 remaining H_2O in the Cm^{3+} hydration shell. This observation is consistent with the broad distribution of Y electron density observed here. TRLFS identifies weak IS sorption (7–8

remaining H_2O) as the dominant species at both investigated pH values. This species is probably consistent with the species that we interpreted as OS species (9 H_2O) in this study. The change in sorption height caused by removing 1 or 2 water from the hydration shell is probably difficult to differentiate by XR. Consistent with the IS complex observed at 1 and 10 mM Y(III) at pH 7 here, Demnitz et al. find a larger contribution of species with < 4 remaining hydration water molecules with increasing pH.[38]

Comparison to other mineral phases. The described sorption behavior can be put into context with other mineral phases. For example, the sorption of Y on orthoclase (001) at pH 5 seems to be similar to the sorption of multivalent cations on muscovite (001).[31,70] While the surface charge of muscovite (001) is mostly pH-independent and therefore the impact of pH on the adsorption of ions is small, this is not true for orthoclase (001). While the surface charge of muscovite (001) is mostly pH-independent and therefore its impact on the adsorption of ions is small, this is not true for orthoclase (001).

The additional contribution of deprotonated TOs to the overall surface charge leads to the increased formation of well-ordered IS complexes of Y^{3+} on orthoclase (001) at near neutral pH. Therefore, the maximum retention of Y^{3+} by orthoclase (θ_{tot} = 1.72 Y^{3+}/nm^2) is higher than by muscovite (θ_{tot} = 1.28 Y^{3+}/nm^2) at the same metal concentration (1 mM). The sorption behavior found for orthoclase at near neutral pH is in fact more similar to the adsorption behavior known for oxide mineral rutile (110) (TiO_2), that adsorbs Y^{3+} predominantly as a tetradentate IS sorption complex.[82]

The results reported in this study clearly demonstrate a very high potential for orthoclase (001) to retain Y^{3+} (θ_{tot} = 2.86 µmol/m^2). This appears to be caused by its two sources of surface charge, release of K^+ and pH-dependent surface site deprotonation. On a fundamental level, we can make a connection between the source of surface charge and dominant sorption speciation. When the orthoclase surface charge is mainly caused by release of cations from the crystal

structure, multivalent ions have been observed to adsorb predominantly in the form of OS complexes.[51] In contrast, IS complexes on orthoclase are preferably formed when surface sites are deprotonated. Orthoclase is unique in this context as its dominant source of surface charge changes with pH. While cation release and OS sorption are found close to the point of zero charge (i.e., pH ~ 2.5[36]), surface site deprotonation and subsequent IS adsorption are found on orthoclase (001) for near-neutral and alkaline pH values (> 6).

3.6. Environmental Implications

Our results improve the current understanding of the retention of trivalent heavy metal ions by K-feldspars on the molecular level. This and previous work showed the high potential of feldspars to retain trivalent heavy metal ions, by an increasing amount of IS sorption with increasing pH.[36,37] The consistency between this study and previous works supports the applicability of the models developed for K-feldspar powders to macroscopic orthoclase crystals, and therefore to more realistic scenarios, which certainly are in between the two extremes studied: mineral powders and gem-quality single crystals. This work shows that the formed molecular species appear to be similar for mineral powders and mineral crystals over large concentrations range, but the total coverage and the ratio of IS to OS species differ due to the different ratio of available sorption sites to metal ions in the aqueous phase.

Therefore, the molecular level findings of this study can be transferred to lower metal concentrations,[83] as they will be present in the environment, for example at REE acid mine drainage sites.[8,12–15] Although the orthoclase (001) cleavage plane investigated here may not be representative for all naturally existing crystal orientations, it will present a significant extent of the exposed surface area.[84] In consequence, the basal planes control adsorption of cations, despite the presence of other more energetically favorable sites, as was previously shown in a computational study on muscovite mica.[43] Overall, the results presented here are therefore

545 closely related to phenomena occurring in some natural systems, e.g. a crystalline rock fracture
546 exposing mm-sized feldspar grains, while providing molecular level structures which can be
547 used to derive reaction equations required for the correct thermodynamic description of the
548 sorption process.
549

Associated content

Supporting Information. Structure of Orthoclase (001) Surface, Experimental Details and Data Analysis of XR Data, Full XR Data Sets and Model Parameters, Alternative Models for RAXR Data, Discussion on Impact of Occupancy of Top K layer, Illustration of (im)possible Binding Motifs of Inner-Sphere Complex, Calculation of Site Deprotonation of Orthoclase (001).

Acknowledgements

This work was primarily funded by the German Federal Ministry of Economics and Technology (BMWi, SMILE project with grant 02E 11668B). Data analysis (by J.N., S.S.L., and P.F.) was supported by the U.S. Department of Energy, Office of Science, Office of Basic Energy Sciences, Chemical Sciences, Geosciences, and Biosciences Division under Contracts DE-AC02-06CH11357 to UChicago Argonne, LLC as operator of Argonne National Laboratory. XR measurements were conducted at GeoSoilEnviroCARS (The University of Chicago, Beamline 13-ID-C), Advanced Photon Source (APS), Argonne National Laboratory which is supported by the National Science Foundation-Earth Sciences (EAR-1634415). J.E.S and P.J.E. received further support from Department of Energy-GeoScience (DE-SC0019108). This research used resources of the Advanced Photon Source, a U.S. Department of Energy (DOE) Office of Science User Facility operated for the DOE Office of Science by Argonne National Laboratory under Contract DE-AC02-06CH11357. M.D. received funding in the frame of the iCross project provided by the German Federal Ministry of Education and Research (BMBF, Grant 02NUK053B) and the Helmholtz Association (Grant SO-093). All authors contributed to the writing of the manuscript.

References

(1) Zapp, P.; Schreiber, A.; Marx, J.; Kuckshinrichs, W. Environmental Impacts of Rare Earth Production. *MRS Bull.* **2022**, *47* (3), 267–275. https://doi.org/10.1557/s43577-022-00286-6.

(2) Jordens, A.; Cheng, Y. P.; Waters, K. E. A Review of the Beneficiation of Rare Earth Element Bearing Minerals. *Miner. Eng.* **2013**, *41*, 97–114. https://doi.org/10.1016/j.mineng.2012.10.017.

(3) Chakhmouradian, A. R.; Wall, F. Rare Earth Elements: Minerals, Mines, Magnets (and More). *Elements* **2012**, *8* (5), 333–340. https://doi.org/10.2113/gselements.8.5.333.

(4) Lawrence, M. G.; Ort, C.; Keller, J. Detection of Anthropogenic Gadolinium in Treated Wastewater in South East Queensland, Australia. *Water Res.* **2009**, *43* (14), 3534–3540. https://doi.org/10.1016/j.watres.2009.04.033.

(5) Kümmerer, K.; Helmers, E. Hospital Effluents as a Source of Gadolinium in the Aquatic Environment. *Environ. Sci. Technol.* **2000**, *34* (4), 573–577. https://doi.org/10.1021/es990633h.

(6) Gutiérrez-Gutiérrez, S. C.; Coulon, F.; Jiang, Y.; Wagland, S. Rare Earth Elements and Critical Metal Content of Extracted Landfilled Material and Potential Recovery Opportunities. *Waste Manag.* **2015**, *42*, 128–136. https://doi.org/10.1016/j.wasman.2015.04.024.

(7) Grawunder, A.; Merten, D.; Büchel, G. Origin of Middle Rare Earth Element Enrichment in Acid Mine Drainage-Impacted Areas. *Environ. Sci. Pollut. Res.* **2014**, *21* (11), 6812–6823. https://doi.org/10.1007/s11356-013-2107-x.

(8) Hao, X.; Wang, D.; Wang, P.; Wang, Y.; Zhou, D. Evaluation of Water Quality in

595 Surface Water and Shallow Groundwater: A Case Study of a Rare Earth Mining Area in
596 Southern Jiangxi Province, China. *Environ. Monit. Assess.* **2016**, *188* (1), 1–11.
597 https://doi.org/10.1007/s10661-015-5025-1.

598 (9) Rim, K. T. Effects of Rare Earth Elements on the Environment and Human Health: A
599 Literature Review. *Toxicol. Environ. Health Sci.* **2016**, *8* (3), 189–200.
600 https://doi.org/10.1007/s13530-016-0276-y.

601 (10) Pagano, G.; Guida, M.; Tommasi, F.; Oral, R. Health Effects and Toxicity Mechanisms
602 of Rare Earth Elements-Knowledge Gaps and Research Prospects. *Ecotoxicol. Environ.*
603 *Saf.* **2015**, *115*, 40–48. https://doi.org/10.1016/j.ecoenv.2015.01.030.

604 (11) Heller, A.; Barkleit, A.; Bok, F.; Wober, J. Effect of Four Lanthanides onto the Viability
605 of Two Mammalian Kidney Cell Lines. *Ecotoxicol. Environ. Saf.* **2019**, *173*, 469–481.
606 https://doi.org/10.1016/j.ecoenv.2019.02.013.

607 (12) Luo, J.; Huo, Y.; Shen, Y.; Hu, J.; Ji, H. Effects of Colloidal Particle Size on the
608 Geochemical Characteristics of REE in the Water in Southern Jiangxi Province, China.
609 *Environ. Earth Sci.* **2016**, *75* (1), 1–17. https://doi.org/10.1007/s12665-015-4870-0.

610 (13) Liu, W. S.; Guo, M. N.; Liu, C.; Yuan, M.; Chen, X. T.; Huot, H.; Zhao, C. M.; Tang,
611 Y. T.; Morel, J. L.; Qiu, R. L. Water, Sediment and Agricultural Soil Contamination
612 from an Ion-Adsorption Rare Earth Mining Area. *Chemosphere* **2019**, *216*, 75–83.
613 https://doi.org/10.1016/j.chemosphere.2018.10.109.

614 (14) Liang, T.; Li, K.; Wang, L. State of Rare Earth Elements in Different Environmental
615 Components in Mining Areas of China. *Environ. Monit. Assess.* **2014**, *186* (3), 1499–
616 1513. https://doi.org/10.1007/s10661-013-3469-8.

617 (15) Ayora, C.; Macías, F.; Torres, E.; Lozano, A.; Carrero, S.; Nieto, J. M.; Pérez-López, R.;

618 Fernández-Martínez, A.; Castillo-Michel, H. Recovery of Rare Earth Elements and
619 Yttrium from Passive-Remediation Systems of Acid Mine Drainage. *Environ. Sci.*
620 *Technol.* **2016**, *50* (15), 8255–8262. https://doi.org/10.1021/acs.est.6b02084.

621 (16) Geckeis, H.; Lützenkirchen, J.; Polly, R.; Rabung, T.; Schmidt, M. Mineral–Water
622 Interface Reactions of Actinides. *Chem. Rev.* **2013**, *113* (2), 1016–1062.
623 https://doi.org/10.1021/cr300370h.

624 (17) Geckeis, H.; Rabung, T.; Schäfer, T. Actinide Nanoparticle Research. In *Actinide*
625 *Nanoparticle Research*; Springer, 2011; pp 1–30. https://doi.org/10.1007/978-3-642-
626 11432-8.

627 (18) Stumpf, S.; Stumpf, T.; Lützenkirchen, J.; Walther, C.; Fanghänel, T. Immobilization of
628 Trivalent Actinides by Sorption onto Quartz and Incorporation into Siliceous Bulk:
629 Investigations by TRLFS. *J. Colloid Interface Sci.* **2008**, *318* (1), 5–14.
630 https://doi.org/10.1016/j.jcis.2007.09.080.

631 (19) García, D.; Lützenkirchen, J.; Petrov, V.; Siebentritt, M.; Schild, D.; Lefèvre, G.;
632 Rabung, T.; Altmaier, M.; Kalmykov, S.; Duro, L.; Geckeis, H. Sorption of Eu(III) on
633 Quartz at High Salt Concentrations. *Colloids Surfaces A Physicochem. Eng. Asp.* **2019**,
634 *578*, 123610. https://doi.org/10.1016/j.colsurfa.2019.123610.

635 (20) Degueldre, C.; Wernli, B. Association Behaviour of ^{241}Am(III) on SiO_2(Amorphous) and
636 SiO_2(Quartz) Colloids. *J. Environ. Radioact.* **1993**, *20* (3), 151–167.
637 https://doi.org/10.1016/0265-931X(93)90007-T.

638 (21) Wilson, R. E.; Schwindt, O.; Fenter, P.; Soderholm, L. Exploitation of the Sorptive
639 Properties of Mica for the Preparation of Higher-Resolution Alpha-Spectroscopy
640 Samples. *Radiochim. Acta* **2010**, *98* (7), 431–436.

https://doi.org/10.1524/ract.2010.1736.

(22) Fenter, P.; Lee, S. S.; Park, C.; Soderholm, L.; Wilson, R. E.; Schwindt, O. Interaction of Muscovite (001) with Pu^{3+} Bearing Solutions at PH 3 through Ex-Situ Observations. *Geochim. Cosmochim. Acta* **2010**, *74* (24), 6984–6995. https://doi.org/10.1016/j.gca.2010.09.025.

(23) Richter, C.; Müller, K.; Drobot, B.; Steudtner, R.; Großmann, K.; Stockmann, M.; Brendler, V. Macroscopic and Spectroscopic Characterization of Uranium(VI) Sorption onto Orthoclase and Muscovite and the Influence of Competing Ca^{2+}. *Geochim. Cosmochim. Acta* **2016**, *189*, 143–157. https://doi.org/10.1016/j.gca.2016.05.045.

(24) Hellebrandt, S.; Lee, S. S.; Knope, K. E.; Lussier, A. J.; Stubbs, J. E.; Eng, P. J.; Soderholm, L.; Fenter, P.; Schmidt, M. A Comparison of Adsorption, Reduction, and Polymerization of the Plutonyl(VI) and Uranyl(VI) Ions from Solution onto the Muscovite Basal Plane. *Langmuir* **2016**, *32* (41), 10473–10482. https://doi.org/10.1021/acs.langmuir.6b02513.

(25) Schmidt, M.; Lee, S. S.; Wilson, R. E.; Soderholm, L.; Fenter, P. Sorption of Tetravalent Thorium on Muscovite. *Geochim. Cosmochim. Acta* **2012**, *88*, 66–76. https://doi.org/10.1016/j.gca.2012.04.001.

(26) Neumann, J.; Qiu, C.; Eng, P.; Skanthakumar, S.; Soderholm, L.; Stumpf, T.; Schmidt, M. Effect of Background Electrolyte Composition on the Interfacial Formation of Th(IV) Nanoparticles on the Muscovite (001) Basal Plane. *J. Phys. Chem. C* **2021**, *125* (30), 16524–16535. https://doi.org/10.1021/acs.jpcc.1c03997.

(27) Blake, R. E.; Walter, L. M. Kinetics of Feldspar and Quartz Dissolution at 70-80°C and near-Neutral PH: Effects of Organic Acids and NaCl. *Geochim. Cosmochim. Acta* **1999**,

664 *63* (13–14), 2043–2059. https://doi.org/10.1016/S0016-7037(99)00072-1.

665 (28) Bezzina, J. P.; Neumann, J.; Brendler, V.; Schmidt, M. Combining Batch Experiments
666 and Spectroscopy for Realistic Surface Complexation Modelling of the Sorption of
667 Americium, Curium, and Europium onto Muscovite. *Water Res.* **2022**, *223* (June),
668 119032. https://doi.org/10.1016/j.watres.2022.119032.

669 (29) Lee, S. S.; Fenter, P.; Park, C.; Sturchio, N. C.; Nagy, K. L. Hydrated Cation Speciation
670 at the Muscovite (001)-Water Interface. *Langmuir* **2010**, *26* (22), 16647–16651.
671 https://doi.org/10.1021/la1032866.

672 (30) Lee, S. S.; Fenter, P.; Nagy, K. L.; Sturchio, N. C. Monovalent Ion Adsorption at the
673 Muscovite (001)-Solution Interface: Relationships among Ion Coverage and Speciation,
674 Interfacial Water Structure, and Substrate Relaxation. *Langmuir* **2012**, *28* (23), 8637–
675 8650. https://doi.org/10.1021/la300032h.

676 (31) Park, C.; Fenter, P. A.; Sturchio, N. C.; Nagy, K. L. Thermodynamics, Interfacial
677 Structure, and PH Hysteresis of Rb^{+} and Sr^{2+} Adsorption at the Muscovite (001)-Solution
678 Interface. *Langmuir* **2008**, *24* (24), 13993–14004. https://doi.org/10.1021/la802446m.

679 (32) Stubbs, J. E.; Legg, B. A.; Lee, S. S.; Dera, P.; De Yoreo, J. J.; Fenter, P.; Eng, P. J.
680 Epitaxial Growth of Gibbsite Sheets on the Basal Surface of Muscovite Mica. *J. Phys.*
681 *Chem. C* **2019**, *123*, 27615–27627. https://doi.org/10.1021/acs.jpcc.9b08219.

682 (33) Schmidt, M.; Lee, S. S.; Wilson, R. E.; Knope, K. E.; Bellucci, F.; Eng, P. J.; Stubbs, J.
683 E.; Soderholm, L.; Fenter, P. Surface-Mediated Formation of Pu(IV) Nanoparticles at
684 the Muscovite-Electrolyte Interface. *Environ. Sci. Technol.* **2013**, *47* (24), 14178–14184.
685 https://doi.org/10.1021/es4037258.

686 (34) Nugent, M. A.; Brantley, S. L.; Pantano, C. G.; Maurice, P. A. The Influence of Natural

687 Mineral Coatings on Feldspar Weathering. *Nature* **1998**, *395* (6702), 588–591.
688 https://doi.org/10.1038/26951.

689 (35) Li, P.; Wu, H.; Liang, J.; Yin, Z.; Pan, D.; Fan, Q.; Xu, D.; Wu, W. Sorption of Eu(III)
690 at Feldspar/Water Interface: Effects of PH, Organic Matter, Counter Ions, and
691 Temperature. *Radiochim. Acta* **2017**, *105* (12), 1049–1058. https://doi.org/10.1515/ract-
692 2017-2797.

693 (36) Neumann, J.; Brinkmann, H.; Britz, S.; Lützenkirchen, J.; Bok, F.; Stockmann, M.;
694 Brendler, V.; Stumpf, T.; Schmidt, M. A Comprehensive Study of the Sorption
695 Mechanism and Thermodynamics of F-Element Sorption onto K-Feldspar. *J. Colloid*
696 *Interface Sci.* **2021**, *591*, 490–499. https://doi.org/10.1016/j.jcis.2020.11.041.

697 (37) Stumpf, S.; Stumpf, T.; Walther, C.; Bosbach, D.; Fanghänel, T. Sorption of Cm(III)
698 onto Different Feldspar Surfaces: A TRLFS Study. *Radiochim. Acta* **2006**, *94* (5), 243–
699 248. https://doi.org/10.1524/ract.2006.94.5.243.

700 (38) Demnitz, M.; Schymura, S.; Neumann, J.; Schmidt, M.; Schäfer, T.; Stumpf, T.; Müller,
701 K. Mechanistic Understanding of Curium(III) Sorption on Natural K-Feldspar Surfaces.
702 *Sci. Total Environ.* **2022**, *843* (May), 156920.
703 https://doi.org/10.1016/j.scitotenv.2022.156920.

704 (39) Stockmann, M.; Schikora, J.; Becker, D. A.; Flügge, J.; Noseck, U.; Brendler, V. Smart
705 Kd-Values, Their Uncertainties and Sensitivities - Applying a New Approach for
706 Realistic Distribution Coefficients in Geochemical Modeling of Complex Systems.
707 *Chemosphere* **2017**, *187*, 277–285. https://doi.org/10.1016/j.chemosphere.2017.08.115.

708 (40) Ochs, M.; Davis, J. A.; Olin, M.; Payne, T. E.; Tweed, C. J.; Askarieh, M. M.; Altmann,
709 S. Use of Thermodynamic Sorption Models to Derive Radionuclide Kd Values for

Performance Assessment: Selected Results and Recommendations of the NEA Sorption Project. In *MIGRATION 2005, 10th international conference on chemistry and migration behaviour of actinides and fission products in the geosphere*; France, 2005.

(41) Payne, T. E.; Davis, J.; Ochs, M.; Olin, M.; Tweed, C. *NEA Sorption Project Phase II: Interpretation and Prediction of Radionuclide Sorption onto Substrates Relevant for Radioactive Waste Disposal Using Thermodynamic Sorption Models*; 2006.

(42) Sassi, M.; Wang, Z.; Walter, E. D.; Zhang, X.; Zhang, H.; Li, X. S.; Tuladhar, A.; Bowden, M.; Wang, H.-F.; Clark, S. B.; Rosso, K. M. Surface Hydration and Hydroxyl Configurations of Gibbsite and Boehmite Nanoplates. *J. Phys. Chem. C* **2020**, *124* (9), 5275–5285. https://doi.org/10.1021/acs.jpcc.0c00659.

(43) Schabernack, J.; Kurganskaya, I.; Fischer, C.; Luttge, A. Influence of Muscovite (001) Surface Nanotopography on Radionuclide Adsorption Studied by Kinetic Monte Carlo Simulations. *Minerals* **2021**, *11* (5), 468. https://doi.org/10.3390/min11050468.

(44) Yuan, T.; Schymura, S.; Bollermann, T.; Molodtsov, K.; Chekhonin, P.; Schmidt, M.; Stumpf, T.; Fischer, C. Heterogeneous Sorption of Radionuclides Predicted by Crystal Surface Nanoroughness. *Environ. Sci. Technol.* **2021**, *55* (23), 15797–15809. https://doi.org/10.1021/acs.est.1c04413.

(45) Cole, W. F.; Sörum, H.; Kennard, O. The Crystal Structures of Orthoclase and Sanidinized Orthoclase. *Acta Crystallogr.* **1949**, *2* (5), 280–287.

(46) Fener, M.; Ince, I. Influence of Orthoclase Phenocrysts on Point Load Strength of Granitic Rocks. *Eng. Geol.* **2012**, *141–142*, 24–32. https://doi.org/10.1016/j.enggeo.2012.05.003.

(47) Fenter, P.; Teng, H.; Geissbühler, P.; Hanchar, J. M.; Nagy, K. L.; Sturchio, N. C.

733 Atomic-Scale Structure of the Orthoclase (001)-Water Interface Measured with High-
734 Resolution X-Ray Reflectivity. *Geochim. Cosmochim. Acta* **2000**, *64* (21), 3663–3673.
735 https://doi.org/10.1016/S0016-7037(00)00455-5.

736 (48) Fenter, P.; Park, C.; Cheng, L.; Zhang, Z.; Krekeler, M. P. S.; Sturchio, N. C. Orthoclase
737 Dissolution Kinetics Probed by in Situ X-Ray Reflectivity: Effects of Temperature, PH,
738 and Crystal Orientation. *Geochim. Cosmochim. Acta* **2003**, *67* (2), 197–211.
739 https://doi.org/10.1016/S0016-7037(02)01084-0.

740 (49) Teng, H. H.; Fenter, P.; Cheng, L.; Sturchio, N. C. Resolving Orthoclase Dissolution
741 Processes with Atomic Force Microscopy and X-Ray Reflectivity. *Geochim.*
742 *Cosmochim. Acta* **2001**, *65* (20), 3459–3474. https://doi.org/10.1016/S0016-
743 7037(01)00665-2.

744 (50) Pollet-Villard, M.; Daval, D.; Fritz, B.; Knauss, K. G.; Schäfer, G.; Ackerer, P. Influence
745 of Etch Pit Development on the Surface Area and Dissolution Kinetics of the Orthoclase
746 (001) Surface. *Chem. Geol.* **2016**, *447*, 79–92.
747 https://doi.org/10.1016/j.chemgeo.2016.09.038.

748 (51) Fenter, P.; Park, C.; Sturchio, N. C. Adsorption of Rb^{+} and Sr^{2+} at the Orthoclase (001)-
749 Solution Interface. *Geochim. Cosmochim. Acta* **2008**, *72* (7), 1848–1863.
750 https://doi.org/10.1016/j.gca.2007.12.016.

751 (52) Stumm, W. *Chemistry of the Solid-Water Interface: Processes at the Mineral-Water and*
752 *Particle-Water Interface in Natural Systems.*; John Wiley & Son Inc.: New York, 1992,
753 1-428.

754 (53) Ishikawa, N. K.; Kuwata, M.; Ito, A.; Umita, T. Effect of PH and Chemical Composition
755 of Solution on Sorption and Retention of Cesium by Feldspar, Illite, and Zeolite as

Cesium Sorbent from Landfill Leachate. *Soil Sci.* **2017**, *182* (2), 63–68.

(54) Liu, Q.; Zhang, X.; Jiang, B.; Li, J.; Li, T.; Shao, X.; Cai, W.; Wang, H.; Zhang, Y. Molecular Dynamics Simulation of Ion Adsorption and Ligand Exchange on an Orthoclase Surface. *ACS Omega* **2021**, *6* (23), 14952–14962. https://doi.org/10.1021/acsomega.1c00826.

(55) Kerisit, S.; Liu, C.; Ilton, E. S. Molecular Dynamics Simulations of the Orthoclase (001)- and (010)-Water Interfaces. *Geochim. Cosmochim. Acta* **2008**, *72* (6), 1481–1497. https://doi.org/10.1016/j.gca.2007.12.014.

(56) Kerisit, S.; Liu, C. Molecular Dynamics Simulations of Uranyl and Uranyl Carbonate Adsorption at Aluminosilicate Surfaces. *Environ. Sci. Technol.* **2014**, *48* (7), 3899–3907. https://doi.org/10.1021/es405387c.

(57) Chardon, E. S.; Livens, F. R.; Vaughan, D. J. Reactions of Feldspar Surfaces with Aqueous Solutions. *Earth-Science Rev.* **2006**, *78* (1–2), 1–26. https://doi.org/10.1016/j.earscirev.2006.03.002.

(58) Robinson, I. K.; Tweet, D. J. Surface X-Ray Diffraction. *Rep. Prog. Phys.* **1992**, *55* (5), 599–651. https://doi.org/10.1088/0034-4885/55/5/002.

(59) Fenter, P.; Park, C.; Nagy, K. L.; Sturchio, N. C. Resonant Anomalous X-Ray Reflectivity as a Probe of Ion Adsorption at Solid-Liquid Interfaces. *Thin Solid Films* **2007**, *515* (14 SPEC. ISS.), 5654–5659. https://doi.org/10.1016/j.tsf.2006.12.118.

(60) Sutton, S. R.; Rivers, M. L.; Chariton, S.; Eng, P. J.; Lanzirotti, A.; Newville, M.; Officer, T.; Prakapenka, V. B.; Ryu, Y. J.; Stubbs, J. E.; Tkachev, S.; Wang, Y.; Wanhala, A.; Xu, J.; Xu, M.; Yu, T.; Zhang, D. GeoSoilEnviroCARS (Sector 13) at the Advanced Photon Source: A Comprehensive Synchrotron Radiation Facility for Earth

779 Science Research at Ambient and Extreme Conditions. *Phys. Chem. Miner.* **2022**, *49* (8),
780 32. https://doi.org/10.1007/s00269-022-01207-4.

781 (61) Trainor, T. P.; Templeton, A. S.; Eng, P. J. Structure and Reactivity of Environmental
782 Interfaces: Application of Grazing Angle X-Ray Spectroscopy and Long-Period X-Ray
783 Standing Waves. *J. Electron Spectros. Relat. Phenomena* **2006**, *150* (2–3), 66–85.
784 https://doi.org/10.1016/j.elspec.2005.04.011.

785 (62) Eikenberry, E. .; Brönnimann, C.; Hülsen, G.; Toyokawa, H.; Horisberger, R.; Schmitt,
786 B.; Schulze-Briese, C.; Tomizaki, T. PILATUS: A Two-Dimensional X-Ray Detector
787 for Macromolecular Crystallography. *Nucl. Instruments Methods Phys. Res. Sect. A*
788 *Accel. Spectrometers, Detect. Assoc. Equip.* **2003**, *501* (1), 260–266.
789 https://doi.org/10.1016/S0168-9002(02)02044-2.

790 (63) Cross, J. O.; Newville, M.; Rehr, J. J.; Sorensen, L. B.; Bouldin, C. E.; Watson, G.;
791 Gouder, T.; Lander, G. H.; Bell, M. I. Inclusion of Local Structure Effects in Theoretical
792 X-Ray Resonant Scattering Amplitudes Using Ab Initio X-Ray-Absorption Spectra
793 Calculations. *Phys. Rev. B* **1998**, *58* (17), 11215–11225.
794 https://doi.org/10.1103/PhysRevB.58.11215.

795 (64) Robinson, I. K. Crystal Truncation Rods and Surface Roughness. *Phys. Rev. B* **1986**, *33*
796 (6), 3830–3836. https://doi.org/10.1103/PhysRevB.33.3830.

797 (65) Fenter, P. A. X-Ray Reflectivity as a Probe of Mineral-Fluid Interfaces: A User Guide.
798 *Rev. Mineral. Geochemistry* **2002**, *49* (1), 149–221.
799 https://doi.org/10.2138/gsrmg.49.1.149.

800 (66) Fenter, P.; Cheng, L.; Park, C.; Zhang, Z.; Sturchio, N. C. Structure of the Orthoclase
801 (001)- and (010)-Water Interfaces by High-Resolution X-Ray Reflectivity. *Geochim.*

802 *Cosmochim. Acta* **2003**, *67* (22), 4267–4275. https://doi.org/10.1016/S0016-
803 7037(03)00374-0.

804 (67) Park, C.; Fenter, P. A. Phasing of Resonant Anomalous X-Ray Reflectivity Spectra and
805 Direct Fourier Synthesis of Element-Specific Partial Structures at Buried Interfaces. *J.*
806 *Appl. Crystallogr.* **2007**, *40* (2), 290–301. https://doi.org/10.1107/S0021889806053131.

807 (68) Schlegel, M. L.; Nagy, K. L.; Fenter, P.; Cheng, L.; Sturchio, N. C.; Jacobsen, S. D.
808 Cation Sorption on the Muscovite (001) Surface in Chloride Solutions Using High-
809 Resolution X-Ray Reflectivity. *Geochim. Cosmochim. Acta* **2006**, *70* (14), 3549–3565.
810 https://doi.org/10.1016/j.gca.2006.04.011.

811 (69) Rudolph, W. W.; Irmer, G. Hydration and Ion Pair Formation in Aqueous Y^{3+}-Salt
812 Solutions. *Dalt. Trans.* **2015**, *44* (42), 18492–18505.
813 https://doi.org/10.1039/c5dt02586a.

814 (70) Lee, S. S.; Schmidt, M.; Laanait, N.; Sturchio, N. C.; Fenter, P. Investigation of
815 Structure, Adsorption Free Energy, and Overcharging Behavior of Trivalent Yttrium
816 Adsorbed at the Muscovite (001)-Water Interface. *J. Phys. Chem. C* **2013**, *117* (45),
817 23738–23749. https://doi.org/10.1021/jp407693x.

818 (71) Shannon, R. D. Revised Effective Ionic Radii and Systematic Studies of Interatomic
819 Distances in Halides and Chalcogenides. *Acta Crystallogr. Sect. A* **1976**, *32* (5), 751–
820 767. https://doi.org/10.1107/S0567739476001551.

821 (72) Walter, M.; Arnold, T.; Geipel, G.; Scheinost, A.; Bernhard, G. An EXAFS and TRLFS
822 Investigation on Uranium(VI) Sorption to Pristine and Leached Albite Surfaces. *J.*
823 *Colloid Interface Sci.* **2005**, *282* (2), 293–305.
824 https://doi.org/10.1016/j.jcis.2004.08.133.

(73) Li, K.; Lian, H.; Shang, M.; Lin, J. A Novel Greenish Yellow-Orange Red Ba3Y4O9:Bi3+,Eu3+ Phosphor with Efficient Energy Transfer for UV-LEDs. *Dalt. Trans.* **2015**, *44* (47), 20542–20550. https://doi.org/10.1039/c5dt03565a.

(74) Zachariasen, W. The Crystal Structure of the Modification C of the Sesquioxides of the Rare Earth Metals, and of Indium and Thallium. *Nor. Geol. Tidsskr.* **1927**, *9* (310–316), 82.

(75) Tan, X.; Fang, M.; Wang, X. Sorption Speciation of Lanthanides/Actinides on Minerals by TRLFS, EXAFS and DFT Studies: A Review. *Molecules* **2010**, *15* (11), 8431–8468. https://doi.org/10.3390/molecules15118431.

(76) Qiu, C.; Majs, F.; Eng, P. J.; Stubbs, J. E.; Douglas, T. A.; Schmidt, M.; Trainor, T. P. In Situ Structural Study of the Surface Complexation of Lead(II) on the Chemically Mechanically Polished Hematite (1-102) Surface. *J. Colloid Interface Sci.* **2018**, *524*, 65–75. https://doi.org/10.1016/j.jcis.2018.04.005.

(77) Qiu, C.; Majs, F.; Douglas, T. A.; Schmidt, M.; Trainor, T. P. In Situ Structural Study of Sb(V) Adsorption on Hematite (1-102) Using X-Ray Surface Scattering. *Environ. Sci. Technol.* **2018**, *52* (19), 11161–11168. https://doi.org/10.1021/acs.est.8b03903.

(78) Lee, S. S.; Heberling, F.; Sturchio, N. C.; Eng, P. J.; Fenter, P. Surface Charge of the Calcite (104) Terrace Measured by Rb+ Adsorption in Aqueous Solutions Using Resonant Anomalous X-Ray Reflectivity. *J. Phys. Chem. C* **2016**, *120* (28), 15216–15223. https://doi.org/10.1021/acs.jpcc.6b04364.

(79) Bellucci, F.; Lee, S. S.; Kubicki, J. D.; Bandura, A.; Zhang, Z.; Wesolowski, D. J.; Fenter, P. Rb+ Adsorption at the Quartz(101) - Aqueous Interface: Comparison of Resonant Anomalous X-Ray Reflectivity with Ab Initio Calculations. *J. Phys. Chem. C*

2015, *119* (9), 4778–4788. https://doi.org/10.1021/jp510139t.

(80) Wang, Z.; Giammar, D. E. Mass Action Expressions for Bidentate Adsorption in Surface Complexation Modeling: Theory and Practice. *Environ. Sci. Technol.* **2013**, *47* (9), 3982–3996. https://doi.org/10.1021/es305180e.

(81) Neumann, J.; Lee, S. S.; Brinkmann, H.; Eng, P. J.; Stubbs, J. E.; Stumpf, T.; Schmidt, M. Impact of Ion-Ion Correlations on the Adsorption of M(III) (M = Am, Eu, Y) onto Muscovite (001) in the Presence of Sulfate. *J. Phys. Chem. C* **2022**, *126* (3), 1400–1410. https://doi.org/10.1021/acs.jpcc.1c09561.

(82) Zhang, Z.; Fenter, P.; Cheng, L.; Sturchio, N. C.; Bedzyk, M. J.; Machesky, M. L.; Wesolowski, D. J. Model-Independent X-Ray Imaging of Adsorbed Cations at the Crystal-Water Interface. *Surf. Sci.* **2004**, *554* (2–3). https://doi.org/10.1016/j.susc.2003.11.047.

(83) Zhao, P.; Begg, J. D.; Zavarin, M.; Tumey, S. J.; Williams, R.; Dai, Z. R.; Kips, R.; Kersting, A. B. Plutonium(IV) and (V) Sorption to Goethite at Sub-Femtomolar to Micromolar Concentrations: Redox Transformations and Surface Precipitation. *Environ. Sci. Technol.* **2016**, *50* (13), 6948–6956. https://doi.org/10.1021/acs.est.6b00605.

(84) Willaime, C.; Christie, J. M.; Kovacs, M.-P. Experimental Deformation of K-Feldspar Single Crystals. *Bull. Minéralogie* **1979**, *102* (2), 168–177. https://doi.org/10.3406/bulmi.1979.7272.